Fast remote spectral discrimination through ghost spectrometry

A. Chiuri,[1,*] M. Barbieri,[2,3] Iole Venditti,[4] Federico Angelini,[1] Chiara Battocchio,[4] Matteo G. A. Paris,[5,6] and Ilaria Gianani[4,†]

[1]*ENEA - Centro Ricerche Frascati, via E. Fermi 45, 00044 Frascati, Italy*
[2]*Dipartimento di Scienze, Universitá degli Studi Roma Tre, Via della Vasca Navale 84, 00146 Rome, Italy*
[3]*Istituto Nazionale di Ottica (INO-CNR), L.go E. Fermi 6, I-50125 Firenze, Italy*
[4]*Dipartimento di Scienze, Università degli Studi Roma Tre, Via della Vasca Navale 84, 00146 Rome, Italy*
[5]*Department of Physics A. Pontremoli, UniversitÃ degli Studi di Milano, I-20133 Milano, Italy*
[6]*Istituto Nazionale di Fisica Nucleare, Sezione di Milano, 20133 Milano, Italy*

(Received 9 November 2023; accepted 15 March 2024; published 12 April 2024)

Assessing the presence of chemical, biological, radiological, and nuclear threats is a crucial task which is usually dealt with in spectroscopic measurements by analyzing the presence of spectral features in a measured absorption profile. The use of quantum ghost spectroscopy opens up the enticing perspective to perform these measurements remotely without compromising the measurement accuracy. However, in order to have the necessary signal-to-noise ratio, long acquisition times are typically required, hence subtracting from the benefits provided by remote sensing. In many instances, though, reconstructing the full spectral lineshape of an object is not needed and the interest lies in ascertaining the presence of a spectrally absorbing object. Here, we present an experimental investigation on the employ of the hypothesis testing framework to obtain a fast and accurate discrimination, carried out by ghost spectrometry. We discuss the experimental results obtained with different samples and complement them with simulations to explore the most common scenarios.

DOI: 10.1103/PhysRevA.109.042617

I. INTRODUCTION

Spectroscopic techniques are a fundamental tool for the characterization of materials [1]. For centuries these have been successfully employed in a variety of fields and have been diversified to account for the most diverse scenarios and needs [2–7]. Incorporating the new capabilities enabled by quantum light has widened the already vast range of possible applications, particularly concerning harnessing quantum frequency correlations [8]. In recent years, two main routes have been pursued. The first exploits spectral correlations between two photons in nondegenerate configurations [9], so that hardly accessible spectral regions can be explored by looking at their correlated counterpart in the visible range [10–12]. The second employs correlations to perform remote sensing measurements [13–15], akin to ghost imaging protocols [16–20]. This latter route represents an advantageous solution when the objects at hand are not easily accessible or constitute a so-called chemical, biological, radiological, and nuclear (CBRN) threat [21]. In these instances it is vital to extract the information at a distance, both to ensure the safety of the users and to ease measurement operations. Although this is also possible using classical spectral correlations, using quantum ones can show a better performance [22–24], especially when the number of modes to be considered is large [25].

Dangerous compounds can be recognized by features in the absorbance spectrum, however, in order to fully retrieve the lineshape of such spectral objects a good signal-to-noise ratio (SNR) is desirable and, given the typical brightness and detection efficiencies, this usually results in long accumulation times. This poses a strong limitation to this technique and dramatically hinders the benefits arising from the use of quantum resources.

If we are interested in swiftly assessing the presence of a threat, retrieving its full lineshape may not be necessary. We may, in fact, recast the problem as a discrimination one, and wonder whether it is possible to infer the presence of the threat comparing a fast low-signal spectral measurement performed on the supposed threat, with a reference measurement. Common techniques for discrimination make use of the correlation coefficient between vectors representing the spectra, or, alternatively, of their distance [26]. These are versatile tests, since no requirements on the distribution are needed; on the other hand, these are prone to artifacts at low SNRs, leading to the wrong attributions.

A decision procedure (an *inference strategy*) prescribes which hypothesis has to be chosen given a set of data. Then, one assigns a *cost* to the choice of the null hypothesis (e.g., no threat) when the alternative hypothesis is true and looks for a strategy minimizing the average cost. In a Bayesian approach, one assigns the equal cost to any wrong inference and zero cost to the correct one, such that the average cost equals the overall probability of error. This approach has been applied to spectroscopy with success [27], but a fully Bayesian approach for large set of data may be challenging. One rather employs

*andrea.chiuri@enea.it
†ilaria.gianani@uniroma3.it

 ©2024 American Physical Society

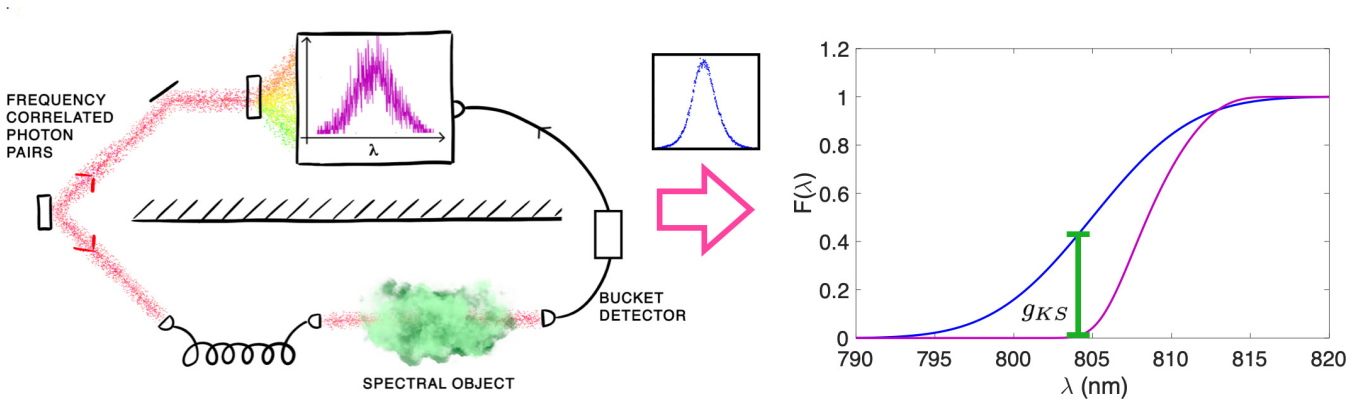

FIG. 1. Conceptual scheme. A ghost-spectrometry scheme is implemented using frequency-correlated photon pairs: one photon is directed toward the supposed location of the spectral object, and detected with a bucket detector, while the other photon is analyzed in frequency. By comparing the recorded coincidences at low SNR with a reference measurement using a Kolmogorov-Smirnov test, it is possible to asses whether the two profiles are samples drawn from the same distribution or not.

the concept of likelihood ratios to evaluate the posterior probabilities.

For binary discrimination problems, where the alternative hypothesis has a low *a priori* probability to occur (i.e., when the threat is not likely to be present), one may also employ the so-called Neyman-Pearson strategy instead of the Bayesian one [28]. The optimal Neyman-Pearson strategy maximizes the probability of revealing the threat when it is there instead of minimizing the probability of error [29]. Following these ideas, we tackle the problem of risk detection by performing a Kolmogorov-Smirnov test (KST) [30] between a high SNR reference and a low SNR measurement with a ghost spectrometer. The KST was specifically developed to test the hypothesis that two samples come from the same distribution and still represents one of the most powerful nonparametric tools of hypothesis testing.

In this work we report an extensive investigation on applying the KST for spectral discrimination based on ghost spectroscopy. We demonstrate an experiment on two different targets and complement our results by simulating different operational regimes. Our results show that even with a slightly absorbing spectral object this technique allows to ascertain the object's presence with a limited number of resources and requiring limited processing on the data, thus enabling time-efficient discrimination.

II. METHOD

Our objective is that of remotely discriminating between the presence or the absence of an object that has an absorption profile in a given spectral range. The object could be, for instance, a CBRN threat that needs to be identified swiftly and whose location cannot be easily accessed. To perform the measurement remotely we consider the quantum ghost spectrometer scheme shown in Fig. 1, by which frequency-correlated photon pairs are generated. One photon is produced in the spectral region where the signatures are expected, sent to the object location, and finally detected by a "bucket" detector with no frequency-resolving capabilities. The second photon, instead, is analyzed locally with a spectrally resolved detection. Due to the frequency correlations between the two photons, the coincidence events between the bucket and the analyzer bear information on the absorption of the object. The appeal of this arrangement is in the fact that one does not need to transport the analysis setup, but only the simpler bucket detector. Under many aspects, this approach is complementary to the one based on induced coherence without induced emission [31]: this allows to further circumvent the need for the bucket detector at the cost of an interferometric scheme [11,12,19,32]. This suggests that ghost spectroscopy may be more suitable for long-distance operation, since this would pose additional experimental challenges for maintaining the necessary phase stability.

The KST for spectral discrimination is based on a three-step scheme. First, we need to define a reliable reference spectrum S_r. We thus perform a calibration measurement with high SNR without any unknown spectral objects. Second, we perform the actual discrimination measurement to ascertain or discard the presence of a spectral object, and record the transmitted spectrum S_s. The different operating conditions will impose a lower SNR, thus making a direct comparison with the reference unpractical, let alone a best fit on an expected shape. We then conclude with the third, last step of the data analysis; the KST allows to follow a model-independent approach, rooted in hypothesis testing. If there were no spectral object, S_s and S_r would have to be two samples drawn from the same distribution. This constitutes our null hypothesis, and we can thus perform the KST to accept or reject this hypothesis: starting from the two measured profiles for the reference S_r and the signal S_s, one builds the two cumulative distributions F_r and F_s and evaluates the quantity

$$g_{KS} = \max_{\lambda} |F_s(\lambda) - F_r(\lambda)|. \tag{1}$$

This corresponds to the maximum separation between the cumulative distribution for the reference (blue) and signal (purple) as illustrated in Fig. 1. The variable g_{KS} is distributed according to a known statistics, whose critical values are found depending on the number of events in S_r and S_s; this allows for a comparison of the samples even with very different sizes. A value of g_{KS} exceeding a set critical value rejects the null hypothesis, thus revealing the presence of an absorbing element; alternatively, the p-value corresponding to

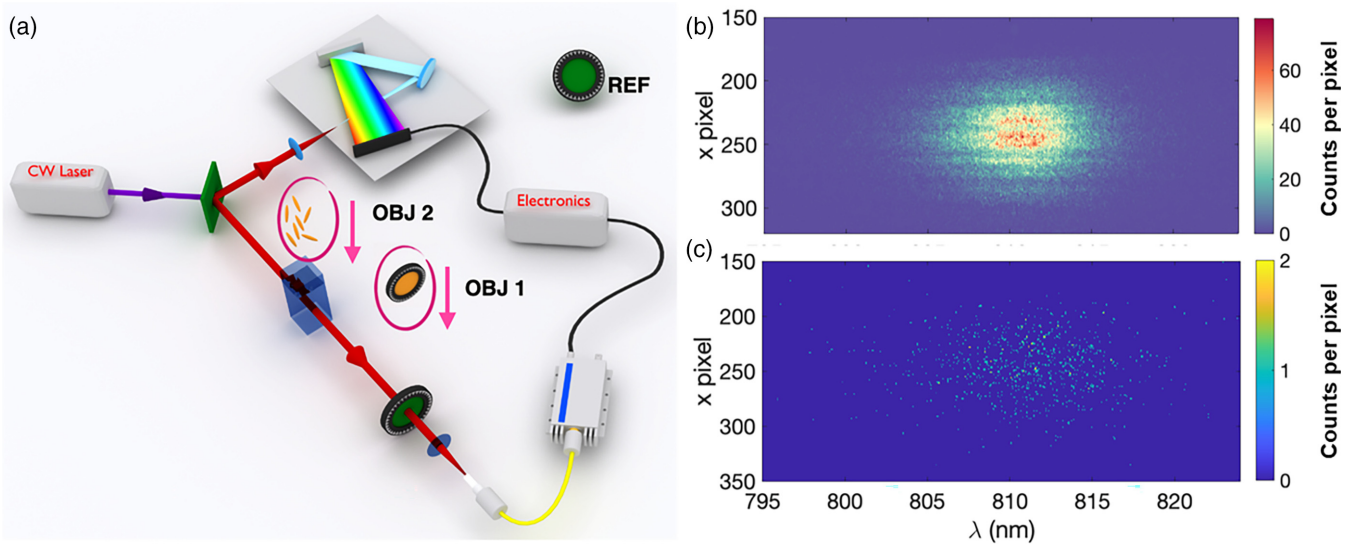

FIG. 2. (a) Experimental setup: A cw 403-nm laser is used to generate photon pairs through SPDC with a 3-mm type-I BBO crystal. One photon is sent through a spectrometer and detected with an intensified CCD camera, while the other photon is sent through a spectral object [either a SGF (orange)] or a solution of gold nanorods (AuNRs) and is detected using a bucket detector. A GBPF (green) acts as a reference. The GBPF is never removed from the setup throughout the two experiments. (b) Recorded coincidences for the reference. (c) Example of recorded coincidences for AuNRs at an accumulation time $t = 10$ s. The wavelength axis refers to the object arm.

the observed g_{KS} can be assessed and contrasted to the desired confidence level. Performing the KST analysis enables us to discriminate the presence of a spectral object in regimes where the reconstruction of the full lineshape would be unfeasible due to the extremely low SNR levels.

III. EXPERIMENT

We explored this approach by means of the setup shown in Fig. 2(a). We employed a cw laser at 403 nm to generate photon pairs through spontaneous parametric down-conversion (SPDC) using a 3-mm-thick type-I Beta barium borate (BBO) crystal.

One photon is directed toward the spectral object and is then detected with an avalanche photodiode (APD, Fast Excelitas SPCM-AQRH-41-FC, corresponding to the bucket detector). The correlated photon is analyzed by a spectrometer (Andor Kymera 328i) and an intensified charge-coupled device (CCD) camera (Andor iStar DH334T-18U-73). A 20-m fiber is used to delay this photon before it reaches the camera: this is needed to allow proper activation of the CCD locked to a trigger from the APD. Fine tuning of this time delay is achieved by means of an Field-Programmable Gate Array (FPGA) board. Our setup allows us to record coincidence events directly, thus measuring the sought spectral distributions.

Figures 2(b) and 2(c) show two examples of detected coincidences for the reference (b) and signal (c). In order to retrieve the spectral profiles these are integrated over the spatial axis, having selected a region of interest. The spectral axis refers directly to the frequencies of the objects, taking into account the correlation. The reference in Fig. 2(b) consists in the spectral profile of a Gaussian bandpass filter (GBPF) centered at 810 nm. The GBPF acts as the reference and is kept fixed throughout all the experiments performed. This mimics the conditions in real applications where it can be useful to limit the observation to a specific bandwidth in which the features are expected. For the calibration step, we aim at reconstructing the reference with good statistics, hence high SNR. By contrast, the events collected in the second step for the signal measurement, Fig. 2(c), appear sparse, and do not form a definite shape, due to the low level of the counts. This is akin to what is expected in remote sensing conditions. Such low SNR is what motivates the employ of the KST.

We first test our technique by using as the spectral object a bandpass fourth-order super-Gaussian filter (SGF) centered at 807 nm with a FWHM of 7.5 nm. We collect the reference spectrum by performing a measurement without any object inserted, but with the GBPF alone, with a long accumulation time ($t = 600$ s) to achieve a good SNR. The reference profile shown in the inset of Fig. 3(a) provides the calibration of the system and, in case of threat detection, it can be performed in a separated safe environment.

Then, keeping the GBPF as the reference, we insert also the spectral object, i.e., the SGF filter, and collect measurements with an accumulation time varying from 1 s to 10 s. Figures 3(b) and 3(c) show the profiles collected at $t = 1$ s and $t = 10$ s. We used the measured profiles to perform the KST, and report the obtained p-values in Fig. 3(a) as a function of the accumulation time. This showcases the advantage of a reduced data collection: even for the signal at $t = 1$ s, which corresponds to a total of 228 detected photons, we were able to reject the null hypothesis with a p-value of 3×10^{-12}. All the values obtained are below the usual thresholds of 1% and 5%, reported in the graph as the dashed and continuous blue lines. While the signal in Fig. 3(b) collected after $t = 1$ s is sufficient to perform the discrimination through the KST analysis, it would be impossible to use the same signal to perform the fitting procedure and the deconvolution needed to extract the lineshape. The discrimination thus occurs on

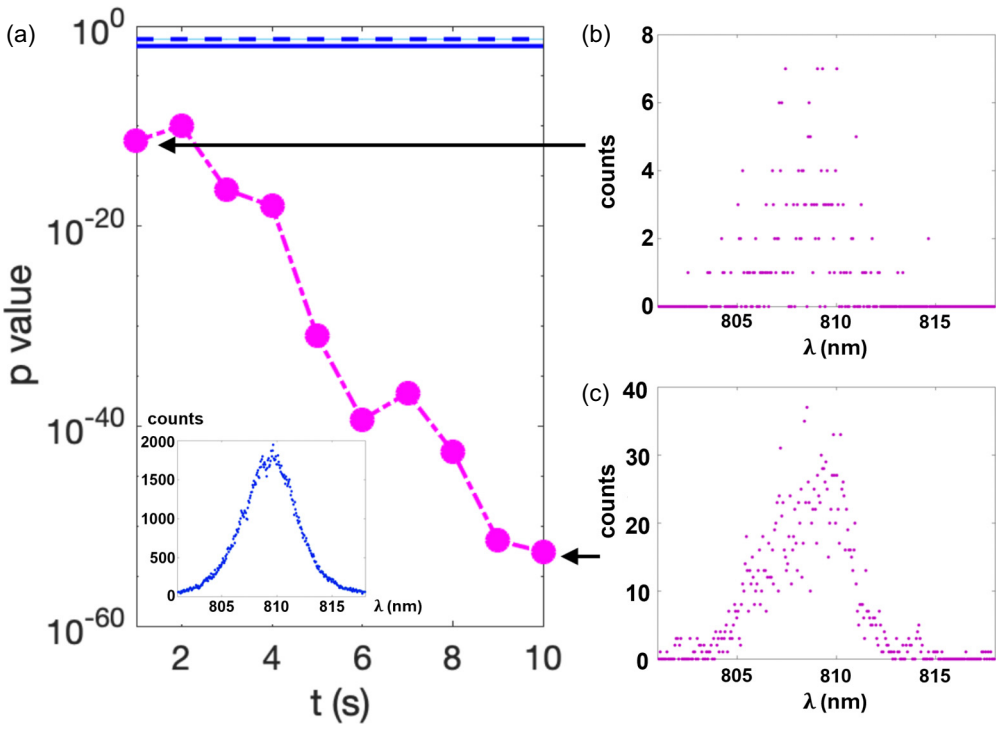

FIG. 3. Results with super-Gaussian filter. (a) Measured p-values obtained from a KS test between the reference (blue inset) and the signal measured with the super-Gaussian filter inserted in the beam at different accumulation times t. The blue dashed and solid lines are the rejection confidence level at 0.05 and 0.01, respectively. (b) and (c) recorded coincidence counts at $t = 1$ s and $t = 10$ s. The wavelength axis refers to the object arm.

much faster time scales than what would be demanded for an appropriate reconstruction of the lineshape.

While this is remarkable given the limited counts required for a successful discrimination, the profile of the object and the reference do differ significantly, having two different shapes and being centered at different wavelengths. This is not necessarily the case in a general scenario, where the spectral object may introduce more subtle discrepancies between the reference and the signal. For this reason, we consider a second spectral object, i.e., a solution of gold nanorods (AuNRs) with a broad surface plasmon resonance band at 695 nm [33]. The reference was collected with the distilled water in a quartz cuvette with a 1-cm path length, selecting the spectral bandwidth as before using the GBPF: this is shown as the blue points in Fig. 4(a). This spectrum is at the tail of the resonance band, therefore the absorption, shown as the orange

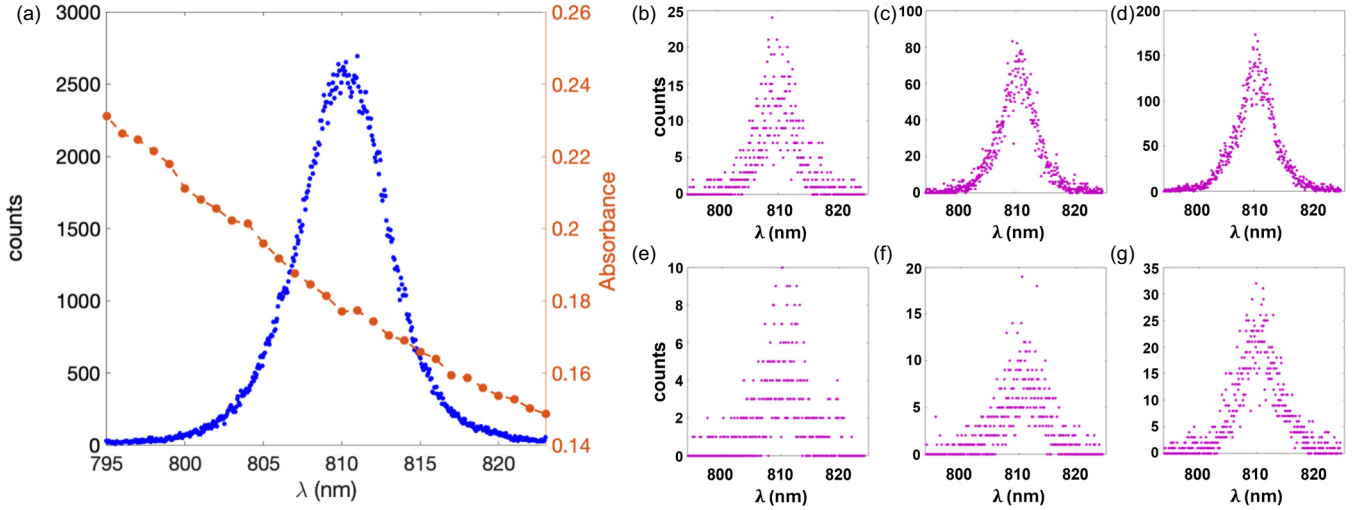

FIG. 4. Nanorod profiles. (a) Reference measurement (blue) and AuNRs absorbance (orange). The absorbance was measured using an UV/VIS spectrophotometer. (b)–(d) C_1 coincidence measurements at $t = 5$, 25, and 50. (e)–(g) C_2 coincidence measurements at $t = 1$, 5, and 10. (b) and (e) correspond to a rejection rate of 0.3, (c) and (f) to a rejection rate of 0.7 for C_1 and 0.8 for C_2, and (d) and (g) to a rejection rate of 0.95. The wavelength axis refers to the object arm.

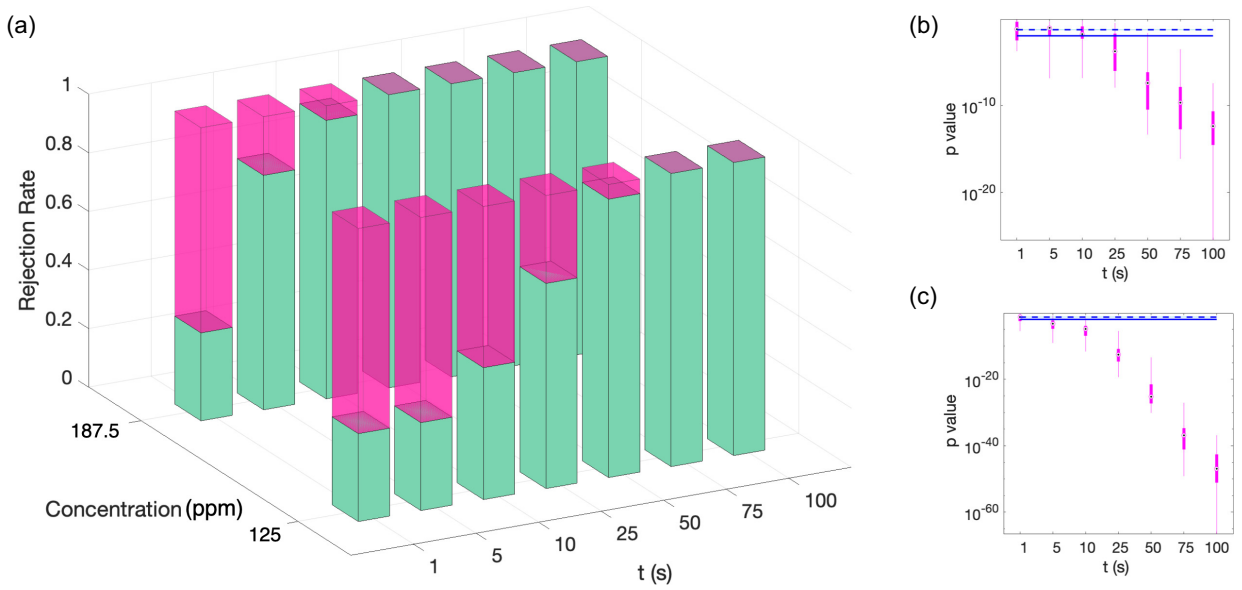

FIG. 5. Results of AuNRs: (a) KS rejection rate for concentration C_1 and C_2. Green bars indicate the successful rejection. Pink bars indicate acceptance of the null hypothesis. (b) p-values for C_1 and (c) p-values for C_2. Blue dashed line: 0.05 confidence level; blue solid line: 0.01 confidence level; the box center indicates the average value, while the box edges indicate the 25th and 75th percentile; the whiskers extend to all measured values.

points in Fig. 4(a), will present a relatively flat spectral behavior, imposing only a slight change to the signal transmitted through the AuNRs with respect to the reference (Fig. 4): the two spectral distributions will differ considerably less than in the previous case. The AuNRs solution was contained in an identical cuvette and we performed the measurement for two different concentrations, $C_1 = 125$ ppm and $C_2 = 188$ ppm, for different accumulation times ranging from $t = 1$ s to $t = 100$ s. In Figs. 4(c)–4(e) we report the profiles for the two concentrations measured for different acquisition times. For each accumulation time we recorded 20 measurements, and for each measurement we ran the KST against the reference. The results are shown in Fig. 5. In Fig. 5(a) we report the rejection rate (green) for the two concentrations at different accumulation times, normalized over the 20 measurements.

The higher concentration results in a spectral distribution which will differ more from the reference compared to the lower concentration. This means that less resources are required for a successful discrimination. On the other hand, the lower concentration is more transparent, hence more resources will be collected per accumulation time. Even by taking this into account, while the rejection rate for C_2 reaches 100% at $t = 25$ s (corresponding to 3000 detected photons), for C_1 the same is achieved at $t = 75$ s (corresponding to 24 000 detected photons). This is reflected in the measured p-values, which are shown in Figs. 5(b) and 5(c) for C_1 and C_2, respectively.

IV. SIMULATIONS

In order to investigate the performance of our approach under typical regimes of operation, we complement the experimental results with numerical simulations. We explore two different scenarios: to provide an ideal benchmark to the example just discussed, we first look at the instance in which the absorption is much broader compared to the spectral region where the reference lies. Such broad spectra usually occur in UV-VIS spectroscopy [34]. We then explore the regime in which the absorption is a narrow line compared to the reference region, as this is the most common occurrence when looking for narrow peaks in the fingerprint region of a IR [35] or in a Raman spectrum [36].

For the first simulation, we consider as a reference a Gaussian envelope $R = \exp[-(\omega - \omega_0)^2/(2\sigma_w^2)]$ centered at $\lambda_0 = 805\,\text{nm} = 2\pi c/\omega_0$, with $\sigma_\lambda = 4\,\text{nm} = 2\pi c\sigma_w/\omega_0^2$, and a spectral object with transmittance $T = 1 - \alpha\lambda$ with α varying between 0 and 0.016 1/nm, as shown in Fig. 6(a). We simulate the measured reference by considering a total of $N_R = 350k$ resources and generating the measured counts by extracting random values from a Poissonian distribution centered at $N_R R$.

The simulated signal is obtained analogously, by multiplying the signal profile by the resources interacting with the spectral object N_T. Since different values of α correspond to a different transmittivity, this will amount to a different number of detected photons depending on the spectral profile. We vary N_T from 300 to 30 000, and for each level of signal we randomly extract 100 simulated profiles and perform a KST for each profile. In Fig. 7 we report the rejection rate normalized over the 100 simulated experiments for varying α and N_T.

When $\alpha = 0$ the signal is equivalent to the reference: indeed, the rejection rate is below 3% at all signal levels. This shows that even with very low signal levels, the absence of the spectral object is almost always correctly detected. The higher the α, the more different the signal distribution from the reference, and the fewer resources are needed for discriminating the two profiles. In Fig. 8 we report the p-values for each α as a function of the number of resources N_T. As expected, for $\alpha = 0$ the p-values are well above the confidence level and as α increases the p-value becomes smaller.

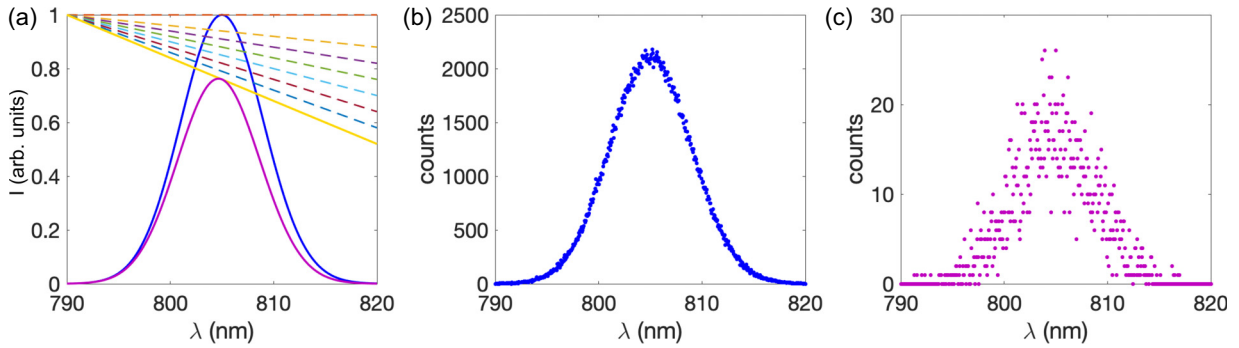

FIG. 6. Simulation broad absorption on a structured reference. (a) Blue: reference, yellow dashed lines: spectral object transmission; purple: signal obtained with the yellow transmission profile. (b) Simulated reference and (c) simulated signal for $\alpha = 0.016$ at the level of signal resulting in a 100% rejection rate.

We now turn to the scenario in which the reference is broader than the absorption feature. We consider a flat reference profile and we model the transmission as $T = 1 - \alpha\{\exp[-(\lambda - \lambda_0)^2/(2\sigma^2)]\}$. We keep $\alpha = 0.2$ fixed and vary the width σ from 0 to 6 nm. The resulting profiles are shown in Fig. 9(a). As before, we simulate the measured reference and the signal; however, given the different profile shape, to attain the same average counts per bin for the reference we now employ $N_R = 600k$ resources. The simulated reference profile is shown in Fig. 9(b). We then simulate the transmitted profile following the same procedure described above, generating 100 simulated profiles for each level of signal and σ. In Fig. 9(c) we show an example of simulated signal relative to the transmission profile with the broadest dip, for $N_T = 15k$ resources. For each generated signal we perform a KST and report the obtained rejection rate in Fig. 10. Even under these unfavorable conditions, dictated by a low absorption ($\alpha = 0.2$) and by a narrow peak, the method achieves satisfactory results, albeit requiring more resources than in the previous instance. In Fig. 11 we report the obtained p-values for each σ as a function of N_T.

V. CONCLUSIONS

In this article we have explored the use of a quantum ghost spectrometer for discriminating the presence of an absorbing spectral object using the Kolmogorov-Smirnov test. We have been able to asses the presence of an object by exploiting a limited amount of resources in an efficient way. We have demonstrated our technique with experiments on two distinct samples, as well as with simulations extending the experimental results to typical spectral regimes.

Our technique provides a viable route for fast discrimination of a spectral object in all the examined conditions. In particular, the more different the spectral profile after the absorption, the fewer resources are needed for a successful discrimination. This makes our technique an optimal solution when dealing with systems that strongly affect the transmission, resulting in exceedingly low signal rates, which, coincidentally, are those that would otherwise require more effort for reconstructing the full lineshape. While the discrimination approach does not require hardware modifications to the conventional ghost spectroscopy apparatus, it takes a

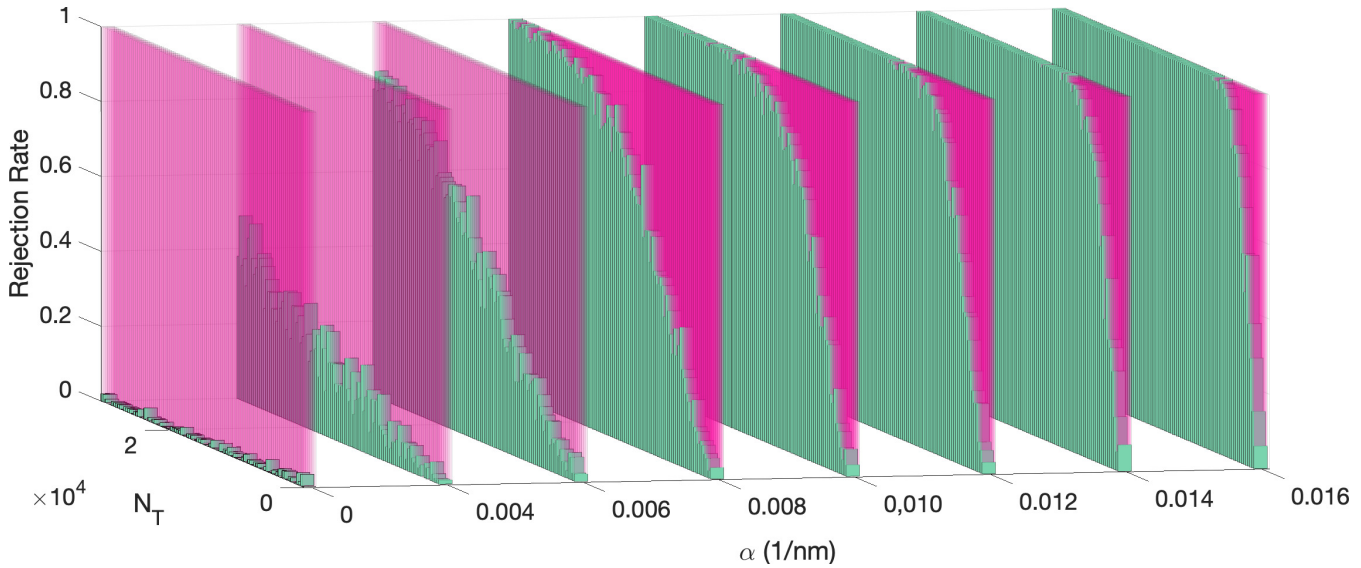

FIG. 7. KS rejection rate for different values of α and resources N_T. Green bars indicate the successful rejection. Pink bars indicate acceptance of the null hypothesis.

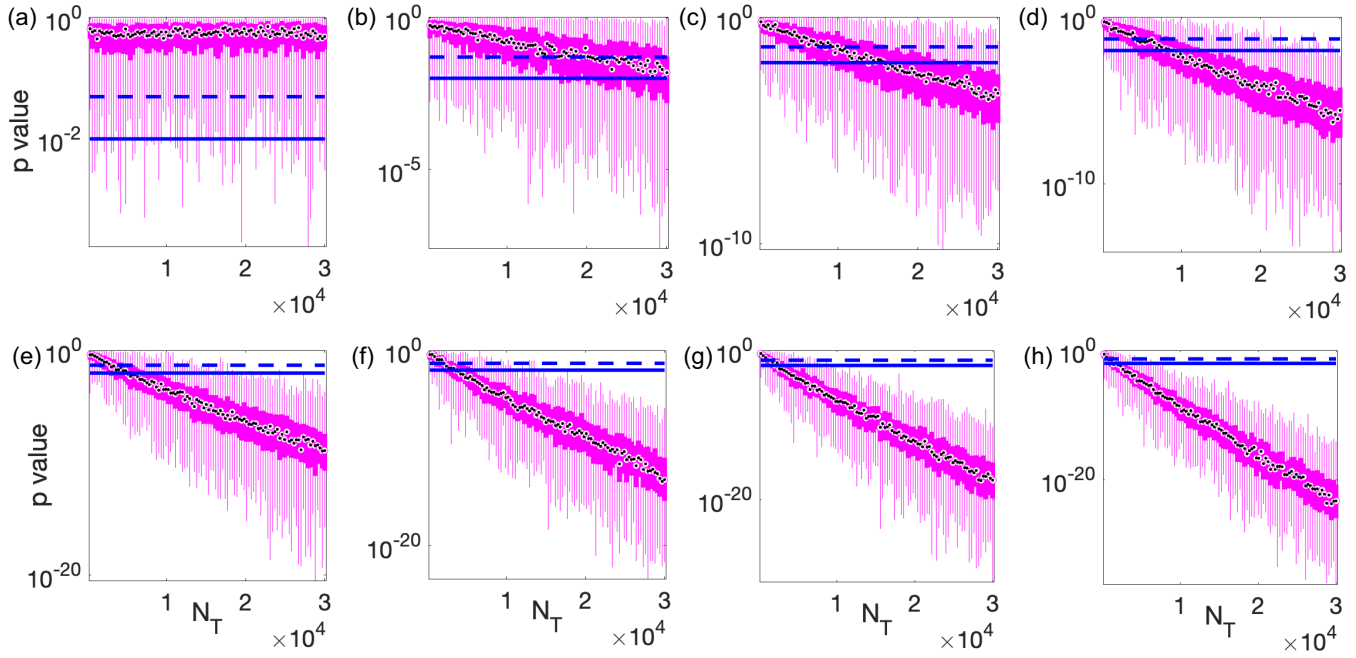

FIG. 8. p-values (a) $\alpha = 0$, (b) $\alpha = 0.004$, (c) $\alpha = 0.006$, (d) $\alpha = 0.008$, (e) $\alpha = 0.010$, (f) $\alpha = 0.012$, (g) $\alpha = 0.014$, and (h) $\alpha = 0.016$. Dashed blue line: 0.05 confidence level; solid blue line: 0.01 confidence level. The box center (black dot) indicates the average value, while the box edges (dark solid pink) indicate the 25th and 75th percentile; the whiskers extend to all measured values.

more sophisticated approach to data analysis, which is key to achieving the sought efficiency. We are persuaded that a more critical and embracing attitude to advanced tools in statistical analysis may prompt the introduction of novel applications beyond what we have demonstrated.

Moreover, our approach can benefit from the control of the phase-matching conditions to ensure operation over large spectral ranges [11,37–39] and in energy nondegenerate emission [32,40–43]. This enables the investigation in otherwise hardly accessible spectral regimes. Before actual remote operation becomes possible, however, the problem of installing and operating the bucket detector to the interested location needs an effective solution; work in this direction is currently underway [44,45].

Our results can be extended in different directions. Solutions taken from fuzzy logic [46] or machine learning algorithms [47] can benefit the hypothesis testing approach. In this respect, machine learning has been employed for classification of nonspectral features [48]. This suggests that the efficiency of the method can be further optimized. As for the extension of the capabilities, incorporating other degrees of freedom, notably, the spatial domain or the polarization, would be particularly helpful in determining not only the presence of a threat but also its position and size.

ACKNOWLEDGMENTS

This work was supported by the NATO Science for Peace and Security (SPS) Programme, project HADES (Project No. G5839) and by the MUR (Grant No. PRIN22-RISQUE-2022T25TR3). M.G.A.P. is partially supported by Grant No. KU-C2PS-8474000137. I.G. acknowledges the support from MUR Dipartimento di Eccellenza 2023-2027. We acknowledge helpful discussions with S. Santoro.

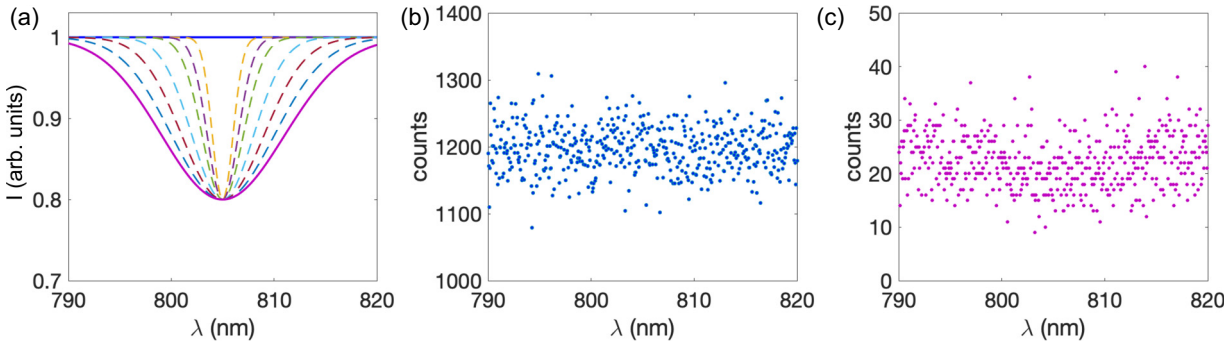

FIG. 9. Simulation for broad reference and narrow absorption. (a) Blue: reference; dashed lines: spectral object transmission; purple: signal obtained with the yellow transmission profile. (b) simulated reference and (c) simulated signal for $\sigma = 6$ nm for $N_T = 15k$, resulting in a 100% rejection rate.

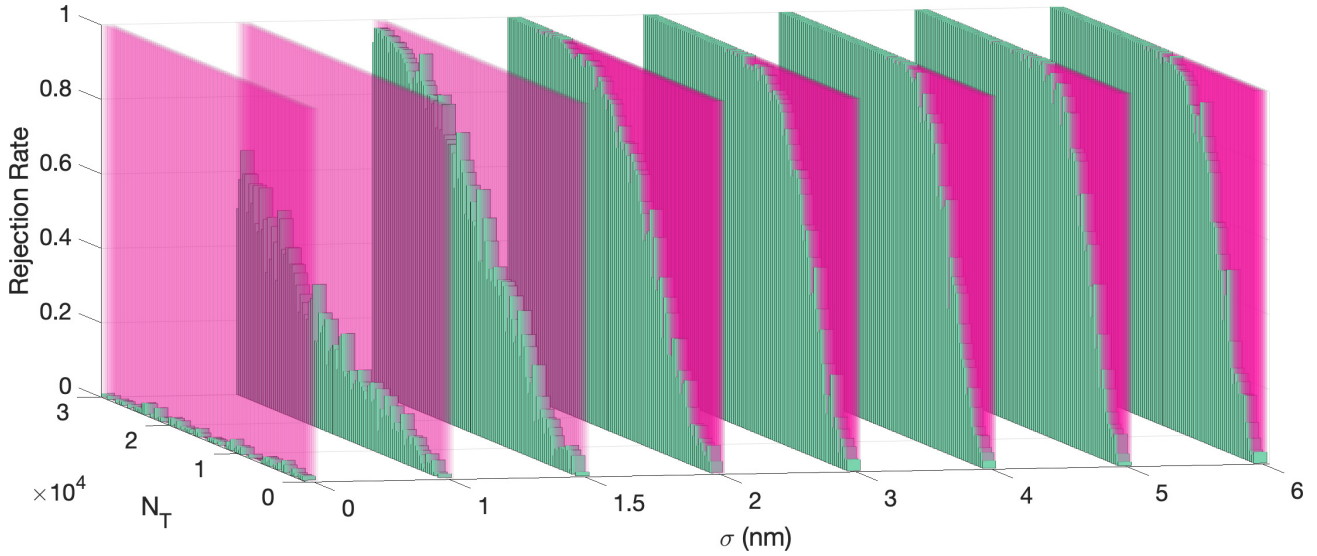

FIG. 10. KS rejection rate for different values of σ and resources N_T. Green bars indicate the successful rejection. Pink bars indicate acceptance of the null hypothesis.

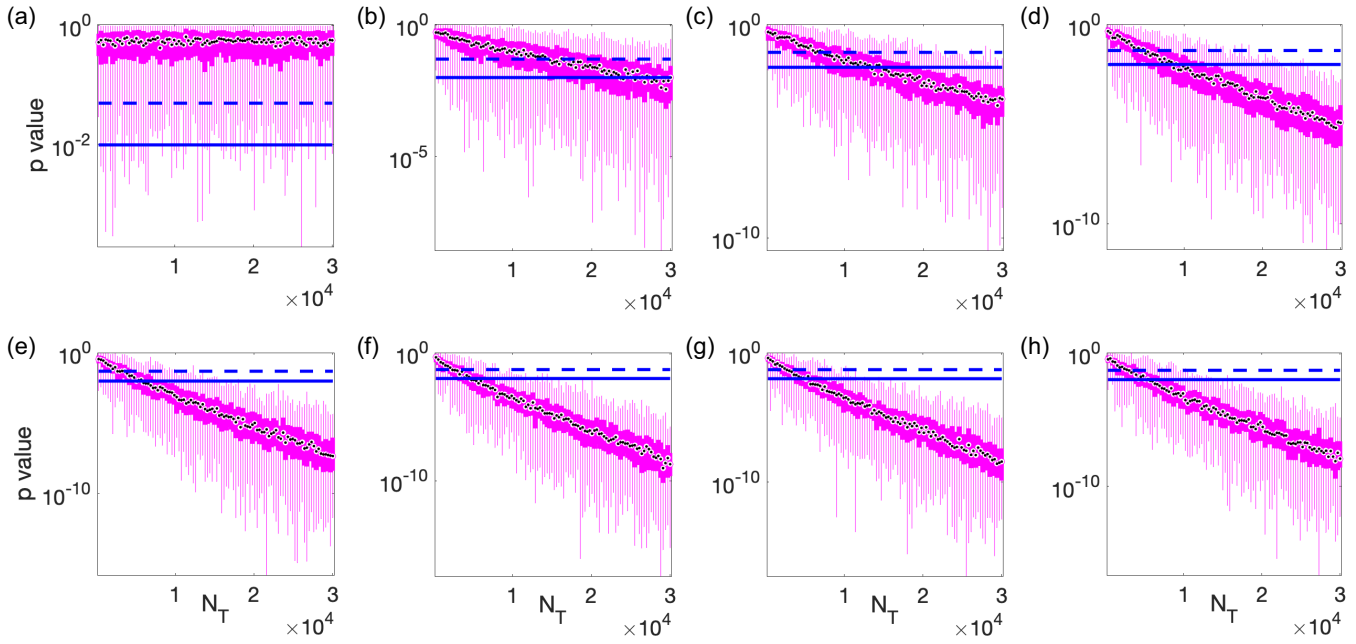

FIG. 11. *p*-values (a) $\sigma = 0$ nm, (b) $\sigma = 1$ nm, (c) $\sigma = 1.5$ nm, (d) $\sigma = 2$ nm, (e) $\sigma = 3$ nm, (f) $\sigma = 4$ nm, (g) $\sigma = 5$ nm, and (h) $\sigma = 6$ nm. Dashed blue line: 0.05 confidence level; solid blue line: 0.01 confidence level. The box center (black dot) indicates the average value, while the box edges (dark solid pink) indicate the 25th and 75th percentile; the whiskers extend to all measured values.

[1] D. L. Pavia, G. M. Lampman, G. S. Kriz, and J. A. Vyvyan, *Introduction to Spectroscopy* (Cengage Learning, Boston, 2014).

[2] C. Koral, G. Papari, and A. Andreone, THz spectroscopy of advanced materials, in *Terahertz (THz), Mid Infrared (MIR) and Near Infrared (NIR) Technologies for Protection of Critical Infrastructures Against Explosives and CBRN*, NATO Science for Peace and Security Series B: Physics and Biophysics, edited by M. F. Pereira and A. Apostolakis (Springer, Dordrecht, 2021), pp. 253–273.

[3] G. G. Hammes, *Spectroscopy for the Biological Sciences* (Wiley, New York, 2005).

[4] M. Adriaens and M. Dowsett, *Spectroscopy, Diffraction and Tomography in Art and Heritage Science* (Elsevier, New York, 2021).

[5] I. Appenzeller, *Introduction to Astronomical Spectroscopy* (Cambridge University, Cambridge, 2012), Vol. 9.

[6] K. Schaefer, *Spectroscopic Atmospheric Environmental Monitoring Techniques* (Society of Photo-Optical Instrumentation Engineers, Bellingham, 1998).

[7] K. Wagatsuma, *Spectroscopy for Materials Analysis: An Introduction* (Springer, New York, 2021).

[8] S. Mukamel, M. Freyberger, W. Schleich, M. Bellini, A. Zavatta, G. Leuchs, C. Silberhorn, R. W. Boyd, L. L. Sánchez-Soto, A. Stefanov, M. Barbieri, A. Paterova, L. Krivitsky, S. Shwartz, K. Tamasaku, K. Dorfman, F. Schlawin, V. Sandoghdar, M. Raymer, A. Marcus *et al.*, Roadmap on quantum light spectroscopy, J. Phys. B: At., Mol. Opt. Phys. **53**, 072002 (2020).

[9] A. A. Kalachev, D. A. Kalashnikov, A. A. Kalinkin, T. G. Mitrofanova, A. V. Shkalikov, and V. V. Samartsev, Biphoton spectroscopy in a strongly nondegenerate regime of SPDC, Laser Phys. Lett. **5**, 600 (2008).

[10] K. W. C. Chan, M. N. O'Sullivan, and R. W. Boyd, Two-color ghost imaging, Phys. Rev. A **79**, 033808 (2009).

[11] D. A. Kalashnikov, A. V. Paterova, S. P. Kulik, and L. A. Krivitsky, Leonid, Infrared spectroscopy with visible light, Nat. Photonics **10**, 98 (2016).

[12] A. V. Paterova, S. M. Maniam, H. Yang, G. Grenci, and L. A. Krivitsky, Hyperspectral infrared microscopy with visible light, Sci. Adv. **6**, eabd0460 (2020).

[13] A. Yabushita and T. Kobayashi, Spectroscopy by frequency-entangled photon pairs, Phys. Rev. A **69**, 013806 (2004).

[14] G. Scarcelli, A. Valencia, S. Gompers, and Y. Shih, Remote spectral measurement using entangled photons, Appl. Phys. Lett. **83**, 5560 (2003).

[15] D. A. Kalashnikov, Z. Pan, A. I. Kuznetsov, and L. A. Krivitsky, Quantum spectroscopy of plasmonic nanostructures, Phys. Rev. X **4**, 011049 (2014).

[16] R. S. Aspden, N. R. Gemmell, P. A. Morris, D. S. Tasca, L. Mertens, M. G. Tanner, R. A. Kirkwood, A. Ruggeri, A. Tosi, R. W. Boyd, G. S. Buller, R. H. Hadfield, and M. J. Padgett, Photon-sparse microscopy: visible light imaging using infrared illumination, Optica **2**, 1049 (2015).

[17] F. V. Pepe, F. Di Lena, A. Garuccio, G. Scarcelli, and M. D'Angelo, Correlation plenoptic imaging with entangled photons, Technologies **4**, 17 (2016).

[18] P. Ryczkowski, M. Barbier, A. T. Friberg, J. M. Dudley, and G. Genty, Ghost imaging in the time domain, Nat. Photonics **10**, 167 (2016).

[19] G. B. Lemos, V. Borish, G. D. Cole, S. Ramelow, R. Lapkiewicz, and A. Zeilinger, Quantum imaging with undetected photons, Nature (London) **512**, 409 (2014).

[20] P.-A. Moreau, E. Toninelli, T. Gregory, and M. J. Padgett, Ghost imaging using optical correlations, Laser Photonics Rev. **12**, 1700143 (2018).

[21] A. Malizia, A. Iannotti, R. Quaranta, R. Rossi, A. Chierici, and C. Russo, 2nd Scientific International Conference on CBRNe SICC Series: 2020: Book of Abstracts, in *2nd Scientific International Conference on CBRNe SICC Series* (TAB, 2020).

[22] M. N. O'Sullivan, K. W. C. Chan, and R. W. Boyd, Comparison of the signal-to-noise characteristics of quantum versus thermal ghost imaging, Phys. Rev. A **82**, 053803 (2010).

[23] R. S. Bennink, S. J. Bentley, R. W. Boyd, and J. C. Howell, Quantum and classical coincidence imaging, Phys. Rev. Lett. **92**, 033601 (2004).

[24] M. J. Padgett and R. W. Boyd, An introduction to ghost imaging: quantum and classical, Philos. Trans. R. Soc. A **375**, 20160233 (2017).

[25] A. Chiuri, I. Gianani, V. Cimini, L. De Dominicis, M. G. Genoni, and M. Barbieri, Ghost imaging as loss estimation: Quantum versus classical schemes, Phys. Rev. A **105**, 013506 (2022).

[26] H. Ghorbani, Mahalanobis distance and its application for detecting multivariate outliers, Facta Univ., Ser.: Math. Info. **34**, 583 (2019).

[27] D. S. Sivia and C. J. Carlile, Molecular spectroscopy and Bayesian spectral analysis—how many lines are there? J. Chem. Phys. **96**, 170 (1992).

[28] I. Maffeis, S. Koudia, A. Gharbi, and M. G. A. Paris, Process estimation in qubit systems: a quantum decision theory approach, Quantum Inf. Process. **18**, 204 (2019).

[29] C. Scott and R. Nowak, A Neyman-Pearson approach to statistical learning, IEEE Trans. Inf. Theory **51**, 3806 (2005).

[30] N. M. Razali and Y. B. Wah, Power comparisons of Shapiro-wilk, Kolmogorov-Smirnov, Lilliefors and Anderson-Darling tests, J. Stat. Modell. Anal. **2**, 21 (2011).

[31] L. J. Wang, X. Y. Zou, and L. Mandel, Induced coherence without induced emission, Phys. Rev. A **44**, 4614 (1991).

[32] I. Kviatkovsky, H. M. Chrzanowski, E. G. Avery, H. Bartolomaeus, and S. Ramelow, Microscopy with undetected photons in the mid-infrared, Sci. Adv. **6**, eabd0264 (2020).

[33] S. Amatori, A. Lopez, C. Meneghini, A. Calcabrini, M. Colone, A. Stringaro, S. Migani, I. Khalakhan, G. Iucci, I. Venditti, and C. Battocchio, Gold nanorods derivatized with CTAB and hydroquinone or ascorbic acid: spectroscopic investigation of anisotropic nanoparticles of different shapes and sizes, Nanoscale Adv. **5**, 3924 (2023).

[34] H.-H. Perkampus, *UV-VIS Spectroscopy and Its Applications* (Springer, Berlin, Heidelberg, 2012).

[35] P. R. Griffiths, J. A. De Haseth, and J. D. Winefordner, *Fourier Transform Infrared Spectrometry* (Wiley, New York, 2007).

[36] P. Rostron, S. Gaber, and D. Gaber, Raman spectroscopy, review, Internatl. J. Eng. Tech. Res. **6**, 2454 (2016).

[37] F. Appas, O. Meskine, A. Lemaître, J. Palomo, F. Baboux, M. I. Amanti, and S. Ducci, Broadband biphoton generation and polarization splitting in a monolithic AlGaAs chip, ACS Photonics **10**, 1136 (2023).

[38] D. Kang, A. Anirban, and A. S. Helmy, Monolithic semiconductor chips as a source for broadband wavelength-multiplexed polarization entangled photons, Opt. Express **24**, 15160 (2016).

[39] R.-B. Jin, R. Shimizu, K. Wakui, H. Benichi, and M. Sasaki, Widely tunable single photon source with high purity at telecom wavelength, Opt. Express **21**, 10659 (2013).

[40] M. Arahata, Y. Mukai, B. Cao, T. Tashima, R. Okamoto, and S. Takeuchi, Wavelength variable generation and detection of photon pairs in visible and mid-infrared regions via spontaneous parametric downconversion, J. Opt. Soc. Am. B **38**, 1934 (2021).

[41] Y. Mukai, R. Okamoto, and S. Takeuchi, Quantum Fourier-transform infrared spectroscopy in the fingerprint region, Opt. Express **30**, 22624 (2022).

[42] A. Vanselow, P. Kaufmann, H. M. Chrzanowski, and S. Ramelow, Ultra-broadband SPDC for spectrally far separated photon pairs, Opt. Lett. **44**, 4638 (2019).

[43] M. Hojo and K. Tanaka, Broadband infrared light source by simultaneous parametric down-conversion, Sci. Rep. **11**, 17986 (2021).

[44] D. Walter, C. Pitsch, G. Paunescu, and P. Lutzmann, Quantum ghost imaging for remote sensing, in *Quantum Communications and Quantum Imaging XVII*, Proc. SPIE (SPIE, 2019), Vol. 11134, pp. 111340W1–7.

[45] C. Pitsch, D. Walter, L. Gasparini, H. Bursing, and M. Eichhorn, 3D quantum ghost imaging, Appl. Opt. **62**, 6275 (2023).

[46] F. Angelini, S. Santoro, and F. Colao, Chemical identification from Raman peak classification using fuzzy logic and Monte Carlo simulation, Chemosensors **10**, 295 (2022).

[47] C. Moodley, A. Ruget, J. Leach, and A. Forbes, Time-efficient object recognition in quantum ghost imaging, Adv. Quantum Technol. **6**, 2200109 (2023).

[48] T. Giordani, A. Suprano, E. Polino, F. Acanfora, L. Innocenti, A. Ferraro, M. Paternostro, N. Spagnolo, and F. Sciarrino, Machine learning-based classification of vector vortex beams, Phys. Rev. Lett. **124**, 160401 (2020).